


Cite this: *Nanoscale*, 2024, **16**, 14861

# A seed-like structured Mo@ZrS<sub>2</sub> catalyst on graphene nanosheets for boosting the performance of rechargeable Zn–air batteries†

Ramasamy Santhosh Kumar,<sup>a</sup> Dilmurod Sayfiddinov,<sup>a</sup> S. Tamilarasi<sup>a</sup> and Dong Jin Yoo  <sup>\*a,b</sup>

Novel composite materials are being studied by researchers for energy storage and renewable energy applications. Here, a seed-like Mo-doped ZrS<sub>2</sub> catalyst was developed on a reduced graphene oxide (rGO) surface by an annealing and hydrothermal method. Using photoelectron spectroscopy, scanning microscopy, and X-ray diffraction analyses, the structure of Mo@ZrS<sub>2</sub>/rGO and the impact of heteroatoms are demonstrated, providing insight into the catalyst. Furthermore, it is demonstrated that Mo@ZrS<sub>2</sub>/rGO has been utilized as an efficient energy storage electrocatalyst by offering a very low half-wave potential of 0.80 V for the oxygen reduction reaction in an alkaline solution. Furthermore, Zn–air batteries with a high-power density of 128.6 mW cm<sup>−2</sup> and exceptional cycling stability are demonstrated by the developed array electrocatalyst. Ultimately, the research findings suggest novel perspectives on the structure of ZrS<sub>2</sub> nanoseeds created by Mo surface doping, promote the usage of Zn–air batteries in practical scenarios, and offer a fascinating idea for creating a redox electrocatalyst.

Received 18th March 2024,

Accepted 6th July 2024

DOI: 10.1039/d4nr01191k

rsc.li/nanoscale

## 1. Introduction

Zinc–air batteries (ZABs) are a promising alternative in modern battery technology due to their excellent theoretical energy density (around 1084 W h kg<sup>−1</sup>), low production cost, and environmental friendliness.<sup>1–4</sup> However, the high polarization and short lifespan of the air electrodes restrict the practical deployment of ZABs. These benefits come naturally from oxygen-based electrochemistry in aqueous systems.<sup>5,6</sup> Consequently, it is critical to create ZAB electrodes that can withstand the slow kinetics of the oxygen evolution reaction (OER) and the oxygen reduction reaction (ORR) during an extended cycling time. Pt and RuO<sub>2</sub>/IrO<sub>2</sub> are two of the precious noble metals that are necessary for the synthesis of modern ORR and OER catalysts.<sup>7–10</sup> More obstacles to the use of scaling are the low abundance, high cost, and inadequate stability of the noble metals.<sup>11–13</sup> Therefore, to advance the use of ZABs, it is essential to use low-cost bifunctional electrocata-

lysts with adequate activity and long-term stability. To date, it has been difficult to find single or bi-metal ZAB catalysts with long cycle lives that can simultaneously offer effective OER and ORR functionalities.<sup>14,15</sup>

A number of noble-metal-free catalysts have demonstrated excellent efficacy in catalyzing these important processes, including transition-metal oxides,<sup>16</sup> chalcogenides,<sup>17</sup> oxynitrides,<sup>18</sup> and their complexes. The development of hybrid catalysts like metal sulfide composites and graphitic carbon frameworks has greatly advanced their potential applications.<sup>19,20</sup> Curiously, when early-transition-metal sulfide nanoparticles were supported by heteroatom-doped carbon or carbon nanotubes, the combined impact of the heteroatom-doped conductive carbon and nanoparticles could produce exceptional ORR activity.<sup>21–23</sup> Similarly, nanoscale metal sulfides show excellent activity and durability for the OER.<sup>24–26</sup> Moreover, doping Zr-based materials with an extra transition metal implies that oxygen from atoms can be readily adsorbed on their surface to speed up ORR kinetics.<sup>19,27</sup> Zr-based catalysts for the ORR, such as carbides, nitrides, and oxides of zirconium, have thus been the subject of extensive investigation.<sup>27,28</sup> For the ORR involving four-electron transfer, Zr-based oxides are thought to be electrocatalytically ineffective due to their innately low electrical conductivity.<sup>29</sup> However, there has not been much research on catalysts based on zirconium sulfide.<sup>25</sup> To increase ORR performances, Zr-based sulfide electrocatalysts exhibiting improved electrical conductivity must be carefully designed.

<sup>a</sup>Department of Energy Storage/Conversion Engineering of Graduate School (BK21 FOUR), Hydrogen and Fuel Cell Research Center, Jeonbuk National University, Jeonju, Jeollabuk-do, 54896 Republic of Korea. E-mail: [djyoo@jbnu.ac.kr](mailto:djyoo@jbnu.ac.kr); Fax: +82-(0) 63-270-3909; Tel: +82-(0) 63-270-3608

<sup>b</sup>Department of Life Science, Jeonbuk National University, Jeonju-si, Jeollabuk-do, 54896 Republic of Korea

† Electronic supplementary information (ESI) available. See DOI: <https://doi.org/10.1039/d4nr01191k>

In this work, on the basis of these outstanding findings, we report a process of doping Mo on the  $\text{ZrS}_2$  seed surface on rGO (reduced graphene oxide) nanosheets ( $\text{Mo@ZrS}_2/\text{rGO}$ ) to produce a sulfur-based ORR catalyst with good performance. Mo was doped on  $\text{ZrS}_2/\text{rGO}$  in a later step after a one-pot process employing Zr and S precursors to produce a  $\text{ZrS}_2/\text{rGO}$  composite with varying atomic ratios. Furthermore, we observed that  $\text{ZrS}_2$  nanoseeds doped with Mo exhibit cutting-edge ORR and ZAB capabilities, demonstrating that Mo is able to both strengthen the contact with  $\text{ZrS}_2$  and modify its electrical properties. Microscopy, diffraction, and photoelectron spectroscopy probes were used to describe the structural and chemical compositions of the produced  $\text{Mo@ZrS}_2/\text{rGO}$  and  $\text{ZrS}_2/\text{rGO}$  catalysts. According to the electrochemical data, the  $\text{ZrS}_2/\text{rGO}$  catalyst with the most active ORR and ZAB performances was synthesised with a lower atomic ratio of Mo. With a half-wave potential of just 0.80 V in a 0.1 M KOH solution, the  $\text{Mo@ZrS}_2/\text{rGO}$  electrocatalyst outperformed ORR electrocatalysts in terms of performance. The rechargeable Zn–air battery assembly for the ORR electrocatalyst demonstrated a remarkable power density and specific capacity of  $128.6 \text{ mW cm}^{-2}$  and  $807.9 \text{ mA h g}^{-1}$ , respectively. This work offers novel findings on the structure of  $\text{Mo@ZrS}_2$  nanoseeds on rGO nanosheets, which is promising for a variety of energy storage applications.

## 2. Experimental

### Materials

Zirconium(IV) oxynitrate dihydrate (Sigma Aldrich, 99%), thiourea (Alfa Aesar, 99%), sodium molybdate dihydrate (Sigma Aldrich, 99.0%), and ammonium fluoride (Sigma Aldrich, 99.99%) were used. Alfa Aesar supplied urea (99.3%), graphite powder (99.99%), and Nafion in 5 weight percentage and 20 weight percent of commercial Pt–C. Samchun Pure Chemicals Co. in South Korea provided both ethanol and potassium hydroxide (KOH).

### Synthesis of $\text{ZrS}_2/\text{rGO}$ and $\text{Mo@ZrS}_2/\text{rGO}$

Using a modified Hummers process, graphite flakes were converted into graphene oxide (GO).<sup>30–32</sup> Typically, 2 mmol  $\text{ZrO}(\text{NO}_3)_2 \cdot 2\text{H}_2\text{O}$ , 4 mmol thiourea, and 10 mg of GO were dissolved in 40 ml of deionized (DI) water. While the mixture was being stirred, 2 mmol ammonium fluoride was introduced into the solution. After stirring for 30 min at room temperature, the solution was transferred to a Teflon-lined hydrothermal autoclave at  $180^\circ\text{C}$  for 4 h. Finally, the obtained material was washed with DI water and ethanol, and then dried at  $60^\circ\text{C}$  for 24 h to produce  $\text{ZrS}_2/\text{rGO}$ .

The synthesis method of  $\text{ZrS}_2/\text{rGO}$  is similar to that of  $\text{Mo@ZrS}_2/\text{rGO}$ . 20 mg of  $\text{ZrS}_2/\text{rGO}$  was dispersed in 40 ml of DI water and sonicated for 10 min. 1 mmol  $\text{Na}_2\text{MoO}_4 \cdot 2\text{H}_2\text{O}$  was added dropwise into pre-dispersed  $\text{ZrS}_2/\text{rGO}$  solution with continuous stirring at room temperature for 1 h. Then, the mixture was introduced into an autoclave for synthesis by the hydrothermal method at  $180^\circ\text{C}$  for 4 h. Following this, the as-

obtained product was washed with DI water and ethanol, and then dried at  $60^\circ\text{C}$  for 24 h. Lastly, the final product was calcined at  $400^\circ\text{C}$  for 2 h to obtain  $\text{Mo@ZrS}_2/\text{rGO}$ . Additionally, the Zn–air battery test, materials, and electrochemical characterization are all described in the ESI† clearly.

## 3. Results and discussion

### Synthesis and characterization of $\text{ZrS}_2/\text{rGO}$ and $\text{Mo@ZrS}_2/\text{rGO}$ nanocatalysts

As shown in Fig. 1a, a hydrothermal and annealing approach were used to synthesise  $\text{ZrS}_2$  on the rGO ( $\text{ZrS}_2/\text{rGO}$ ) utilizing metal-precursors namely zirconium oxynitrate and thiourea in a sample of GO solution. Strong contacts between the GO sheet and the metal precursors are produced by the functional groups present in the GO.<sup>34</sup> The absorbed metal precursors consistently formed a seed-like structured  $\text{ZrS}_2$  on rGO during the hydrothermal reaction, and at the same time, GO was converted into rGO since thiourea was present. In the present study, the structure-tuning agent employed to regulate the production of the  $\text{ZrS}_2$  nanocatalyst with a seed-like structure was ammonium fluoride. Consequently, as seen in Fig. S1a–d,† the FE-SEM (field emission scanning electron microscopy) images of  $\text{ZrS}_2/\text{rGO}$  reveal the seed-like structure of  $\text{ZrS}_2$  growing on the rGO sheet. The extra atom needs to be doped in order to enhance the physical interaction of  $\text{ZrS}_2/\text{rGO}$  nanocatalysts that show enhanced electrical conductivity. As a result, we have doped the Mo atom on the  $\text{ZrS}_2/\text{rGO}$  nanocatalyst surface here using  $\text{Na}_2\text{MoO}_4$  as the precursor Mo atom dopant. Because, as shown in Fig. S1e and f,† the addition of a Mo atom to the  $\text{ZrS}_2/\text{rGO}$  nanocatalyst did not harm the seed-like structure, the addition caused the nanoparticle to form on the seed-like structure ( $\text{Mo@ZrS}_2/\text{rGO}$ ). Moreover, the elemental analysis of energy dispersive X-ray (EDS) spectroscopy verified the presence of every species in the final catalyst and showed that Mo had been successfully deposited (Fig. S1g†). We firmly expect that the doped atom will enhance the catalytic activity and form robust chemical bonds with Zr–S atoms, and rGO functional groups since the contact between metals (Mo–Zr) facilitates catalytic reactions.

Moreover, as shown in Fig. 1b, Raman spectroscopy was used to illustrate the graphitic and defective surroundings of GO,  $\text{ZrS}_2/\text{rGO}$ , and  $\text{Mo@ZrS}_2/\text{rGO}$  composites. Two prominent peaks in the Raman spectra of graphitic oxide (GO) may be seen at  $1352.8$  and  $1580.7 \text{ cm}^{-1}$ , respectively. These peaks correspond to the D and G bands, which denote the defect structure of carbon graphitic and the  $\text{sp}^2$  character of carbon atoms. The fact that the  $I_D/I_G$  values of GO, at roughly 0.99, were lower compared to those of  $\text{ZrS}_2/\text{rGO}$  and  $\text{Mo@ZrS}_2/\text{rGO}$  ( $I_D/I_G = 1.09$  and  $1.05$ , respectively) indicates that the synthesis of both catalysts was successful.<sup>35</sup> The further peaks at  $832$  and  $985 \text{ cm}^{-1}$  were due to Mo doping in the final catalyst,<sup>36</sup> while the development of peaks at  $460$  and  $621 \text{ cm}^{-1}$  suggests that  $\text{ZrS}_2$  was successfully deposited onto rGO.<sup>37</sup>  $\text{ZrS}_2$  and  $\text{Mo@ZrS}_2$  have successfully formed on a rGO nanocomposite, according to these findings.

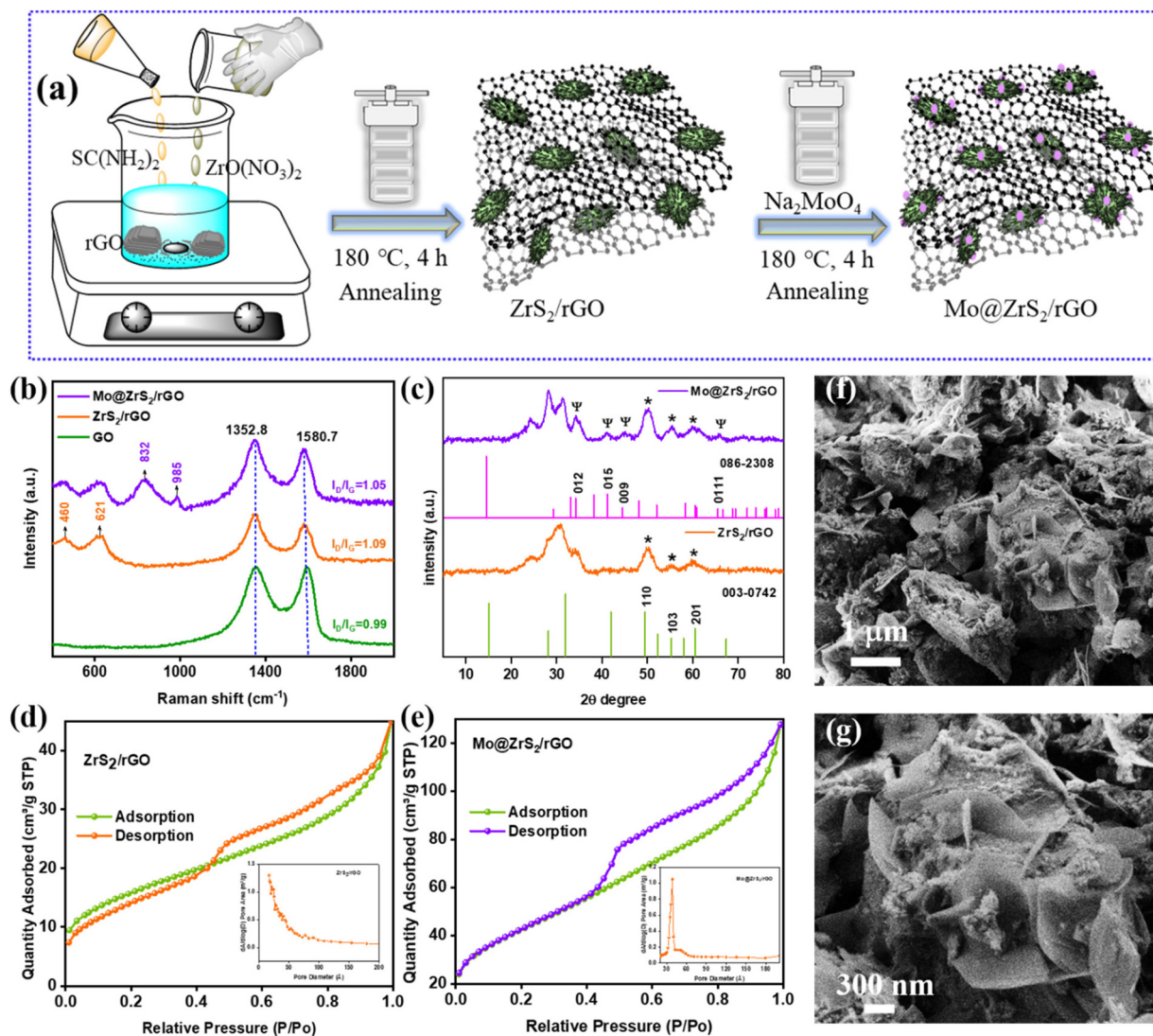


**Fig. 1** (a) Schematic illustration of the synthesis of  $\text{ZrS}_2/\text{rGO}$  and  $\text{Mo@ZrS}_2/\text{rGO}$  nanocomposites. (b) Raman spectra, (c) XRD patterns, (d and e)  $\text{N}_2$  sorption isotherms of  $\text{ZrS}_2/\text{rGO}$  and  $\text{Mo@ZrS}_2/\text{rGO}$  nanocomposites, and (f and g) SEM images of the  $\text{Mo@ZrS}_2/\text{rGO}$  nanocomposite.

Moreover, the crystal structure characteristics of  $\text{ZrS}_2/\text{rGO}$  and  $\text{Mo@ZrS}_2/\text{rGO}$  were examined using X-ray diffraction (XRD). The  $\text{ZrS}_2/\text{rGO}$  and  $\text{Mo@ZrS}_2/\text{rGO}$  samples showed a large peak (002) at  $30.3^\circ$ , which is typically connected to the rGO plane. This observation confirms that GO has been effectively reduced to rGO (Fig. 1c). The XRD pattern shows small peaks of  $\text{ZrS}_2$  at  $50.0$ ,  $55.2$ , and  $59.7^\circ$  appropriate to the (1 1 0), (1 0 3), and (2 0 1) planes, respectively. JCPDS-003-0742 shows that the diffraction pattern of these peaks is a regular, characteristic  $\text{ZrS}_2/\text{rGO}$  (hexagonal structure with the  $P\bar{3}m1$  space group).<sup>38</sup> However, after Mo was added to produce the final catalyst, each peak of  $\text{ZrS}_2$  and rGO grew more distinct. Moreover, a low-intensity peak corresponding to Mo appeared at  $34.1$ ,  $41.1$ ,  $44.4$ , and  $65.5^\circ$  indicating the (0 1 2), (0 1 5), (0 0 9), and (0 1 11) planes, respectively.<sup>39</sup> The diffraction pattern of these peaks corresponds to the regular, distinctive  $\text{Mo@ZrS}_2/\text{rGO}$  (rhombohedral structure with the  $R\bar{3}m$  space

group), as demonstrated by JCPDS-086-2308. The crystal planes showed plenty of heteroatom production on the rGO nanosheet and were confirmed by HR-TEM (high resolution-transmission electron microscopy) images. Furthermore, Brunauer–Emmett–Teller (BET) analysis was used to examine the large surface area of the seed-like structured  $\text{ZrS}_2/\text{rGO}$  ( $56.0 \text{ cm}^2 \text{ g}^{-1}$ ) and  $\text{Mo@ZrS}_2/\text{rGO}$  ( $150.8 \text{ cm}^2 \text{ g}^{-1}$ ) nanocatalyst (Fig. 1d and e). Furthermore, the resulting seed-like structured  $\text{Mo@ZrS}_2/\text{rGO}$  nanocatalyst exhibits a pore diameter in the range of  $52.3$  and  $49.0 \text{ \AA}$ , according to the BJH pore size distribution (Fig. 1d and e insert image), which is very advantageous for the charge-transfer phase of electrocatalytic activity. Consequently, the  $\text{Mo@ZrS}_2/\text{rGO}$  nanocatalyst with a seed-like structure exhibits a large surface area for Mo atoms with a spherical shape that are dispersed on  $\text{ZrS}_2$  seeds (Fig. 1f and g).

In addition to the perfect seed-like structured  $\text{Mo@ZrS}_2$  nanocatalyst on the developing rGO surface, the morphology



was studied using images from transmission electron microscopy (TEM). The production of seed-like structures that were evenly distributed across the outermost layer of rGO nanosheets is evident in Fig. S3a and b.† Moreover, the size of the seed-like structured Mo@ZrS<sub>2</sub> nanocatalyst was determined utilizing the results of individual histograms. On the outermost layer of rGO containing active sites, this revealed a mean length spacing of nanoseeds with an average particle diameter size of around 190 nm (Fig. 2a and b). The HR-TEM analysis of the seed-like structured Mo@ZrS<sub>2</sub> nanocatalyst is presented in Fig. 2c and d. These images demonstrate the presence of distinct lattice fringes, measuring approximately 0.316 and 0.293 nm in equivalent crystalline size. The associated crystalline peaks are assigned to the (100) and (006) planes, respectively. Fig. S2a–c† illustrates the interparticle link between neighboring seed-like organized Mo@ZrS<sub>2</sub> nanocatalysts. Through electrocatalysis, interparticle structures can enhance electron transfer across the seed-like structures, sustain mechanical strength, and confirm heteroatom formation.<sup>17</sup>

Moreover, the fast Fourier transform (FFT) and selected area electron diffraction (SAED) patterns verified the creation of a seed-like ordered Mo@ZrS<sub>2</sub> nanocatalyst through polycrystalline structures (insert image; Fig. 2c and d). As seen in the Fig. 2d inset image, distinct lattice edges were found to have a

*d*-spacing of 0.317 nm correlating with the (100) layer of Mo@ZrS<sub>2</sub>. TEM-EDS-elemental mapping in Fig. 2e and f, and S3c† demonstrated the successful doping of the Mo atom inside the novel structure of the seed-like ZrS<sub>2</sub>/rGO nanocatalyst. By using high-angle annular dark-field scanning transmission electron microscopy (HAADF-STEM) imaging, the uniform distribution of Mo, Zr, S, O, and C elements was also determined. This demonstrated that the elements of Mo@ZrS<sub>2</sub> nanocatalysts were similarly distributed across the rGO surface. Furthermore, Mo and Zr ratios in the product were found to be 1 : 3 by energy-dispersive X-ray (EDX) spectroscopy, as is seen in Fig. S3d.†

X-ray photoelectron spectroscopy (XPS) was used to confirm the chemical composition and binding states of Mo@ZrS<sub>2</sub>/rGO and ZrS<sub>2</sub>/rGO composites. The XPS spectra show that distinct peaks were dispersed throughout the rGO sheet for each element in the ZrS<sub>2</sub>/rGO and Mo@ZrS<sub>2</sub>/rGO composites. In addition, as illustrated in Fig. 3a, the survey spectrum determines the elemental compositions of the ZrS<sub>2</sub>/rGO and Mo@ZrS<sub>2</sub>/rGO samples, which comprise C, O, Zr, S, and extra Mo in the following sample. Specifically, ZrS<sub>2</sub>/rGO contains 44.4% carbon, 42.94% oxygen, 10.9% zirconium, and 1.72% sulfur, whereas Mo@ZrS<sub>2</sub>/rGO contains 48.14% carbon, 41.07% oxygen, 8.24% zirconium, 1.06% sulfur, and 1.49% molybdenum (inset image; Fig. 3a).

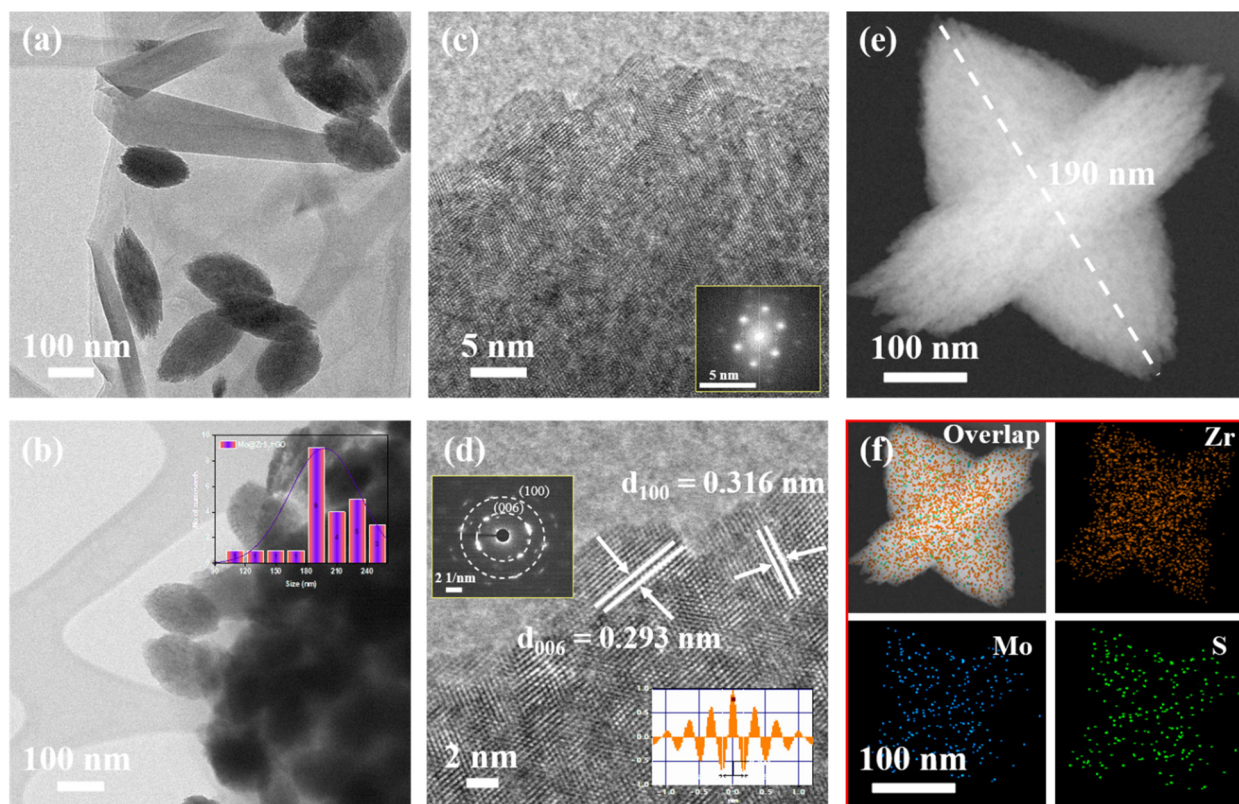


**Fig. 2** TEM analysis of the Mo@ZrS<sub>2</sub>/rGO nanocomposite; (a and b) TEM images (inset image; size distribution of seed structures), (c and d) HR-TEM images, (inset image; FFT pattern, SAED, and lattice spacings of 006 and 100 planes), (e) HAADF-STEM image, and (f) TEM-EDS elemental mapping images of Zr, Mo, and S elements, respectively.

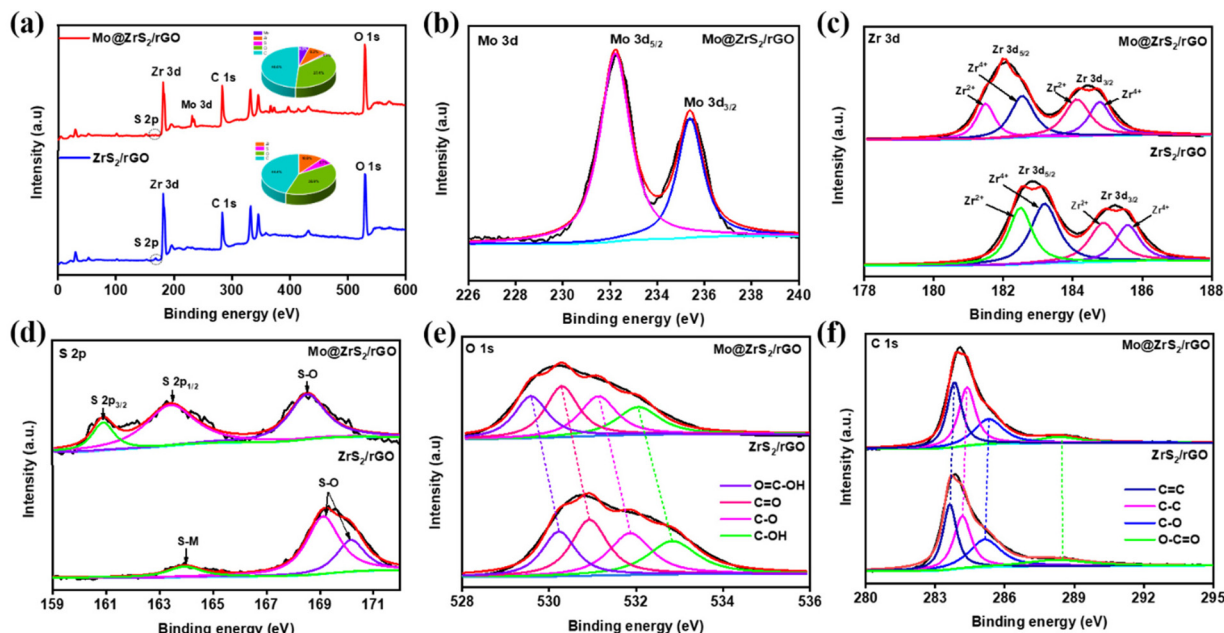


**Fig. 3** XPS analysis of  $\text{ZrS}_2/\text{rGO}$  and  $\text{Mo@ZrS}_2/\text{rGO}$  nanocomposites: (a) survey spectra and high-resolution XPS spectra of (b) Mo 3d, (c) Zr 3d, (d) S 2p, (e) O 1s, and (f) C 1s.

The final synthesized catalyst was found to contain Mo 3d doublets ( $3d_{5/2}$  and  $3d_{3/2}$ ) with high-resolution binding energies of 232.3 and 235.4 eV, respectively (Fig. 3b).<sup>40–42</sup> The presence of  $\text{ZrS}_2$  and  $\text{ZrS}$  in  $\text{ZrS}_2/\text{rGO}$  is confirmed by the peaks seen at 182.8 and 185.2 eV, which can be attributed to  $\text{Zr } 3d_{5/2}$  and  $\text{Zr } 3d_{3/2}$ , respectively.<sup>43,44</sup> In line with predictions, these peaks moved to 182.1 and 184.5 eV when Mo was added, signifying the creation of  $\text{MoZrS}_2/\text{rGO}$ , which are shown in Fig. 3c. The addition of Mo to  $\text{Mo@ZrS}_2/\text{rGO}$  causes an increase in the sulfur–metal bonding peaks, which appear as S  $2p_{3/2}$  and S  $2p_{1/2}$  at 160.9 and 163.4 eV, respectively.<sup>41,45</sup> The high-resolution S 2p spectrum shows a low ratio of sulfur–metal bonding in  $\text{ZrS}_2/\text{rGO}$  (Fig. 3d). However, as can be seen in Fig. 3e, the inclusion of Mo dramatically changes the binding energy of the O 1s spectrum: for O=C–OH, C=O, C–O, and C–OH, respectively, it shifts from 529.6, 530.3, 531.1, and 532.1 eV to 530.2, 530.9, 531.9, and 532.1 eV.<sup>9</sup> According to the high-resolution C 1s spectra study,  $\text{ZrS}_2/\text{rGO}$  bonds with C=C, C–C, C–O, and O–C=O at 283.6, 284.2, 285.2, and 288.5 eV, in that order (Fig. 3f).<sup>9,30</sup> Furthermore, the C 1s spectrum is barely altered by the addition of Mo to  $\text{ZrS}_2/\text{rGO}$ . Ultimately, our investigations verified that the rGO nanosheets were successfully formed from a seed-like structure. This suggests that nanocatalysts can enhance the electrochemical activity for applications using ORR and ZABs.

#### Evaluate the ORR performance of $\text{ZrS}_2/\text{rGO}$ and $\text{Mo@ZrS}_2/\text{rGO}$ nanocatalysts

The ORR performance of  $\text{ZrS}_2/\text{rGO}$ ,  $\text{Mo@ZrS}_2/\text{rGO}$ , and commercial Pt–C electrodes was investigated to explore the electrocatalytic activity in addition to having excellent cyclic dura-

bility. The electrocatalytic efficiency of the catalysts that were synthesized for the ORR was investigated using cyclic voltammograms (CVs) using 0.1 M KOH that were saturated with  $\text{N}_2$  and  $\text{O}_2$ . However, when the electrolyte was saturated with  $\text{O}_2$ , distinct cathodic reduction peaks emerged (Fig. 4a and S4a†), where the ORR electrocatalytic efficiency is represented by the strength and location of the reduction peaks. For the catalysts that were in the  $\text{N}_2$  saturated solution, there was no reduction peak.  $\text{Mo@ZrS}_2/\text{rGO}$  demonstrated superior ORR performance, with a bigger higher peak potential at  $\approx 0.80$  V compared to the remaining catalysts ( $\text{ZrS}_2/\text{rGO}$ ; 0.76 V), apart from Pt–C ( $\approx 0.85$  V). The various catalysts were subjected to linear sweep voltammograms (LSVs) utilizing an oscillating disk electrode (RDE) in a 0.1 M  $\text{O}_2$ -saturated solution of KOH at different rotation speeds (400 to 2800 rpm) as shown in Fig. S4b–d.† Unless otherwise indicated, the blank response that was recorded under  $\text{N}_2$  was used to adjust the current density. The onset potential ( $E_{\text{onset}} = 0.86$  V) and half-wave potential ( $E_{1/2} = 0.76$  V) of  $\text{ZrS}_2/\text{rGO}$  are comparatively lower than those of the other materials, as shown in Fig. 4b at 1600 rpm. This difference in ORR activity may be due to the presence of the stable state ( $\text{Zr}^{4+}$ ) in the active region and the significant aggregation of  $\text{ZrS}_2/\text{rGO}$  throughout electrochemical testing. However, the highly conductive GO significantly increased the  $E_{\text{onset}}$  and  $E_{1/2}$  of  $\text{ZrS}_2/\text{rGO}$  and also prevented the aggregation of  $\text{ZrS}_2$ .

Additionally, compared to  $\text{ZrS}_2/\text{rGO}$ ,  $\text{Mo@ZrS}_2/\text{rGO}$  exhibits somewhat better  $E_{\text{onset}}$  (0.88 V) and  $E_{1/2}$  (0.80 V). This is largely because Mo-doped  $\text{ZrS}_2$  forms a large number of active locations ( $\text{Mo}^{4+}$  state) for an effective ORR. When compared to the remaining synthesis materials,  $\text{Mo@ZrS}_2/\text{rGO}$  showed superior values, which are very similar to commercial Pt–C

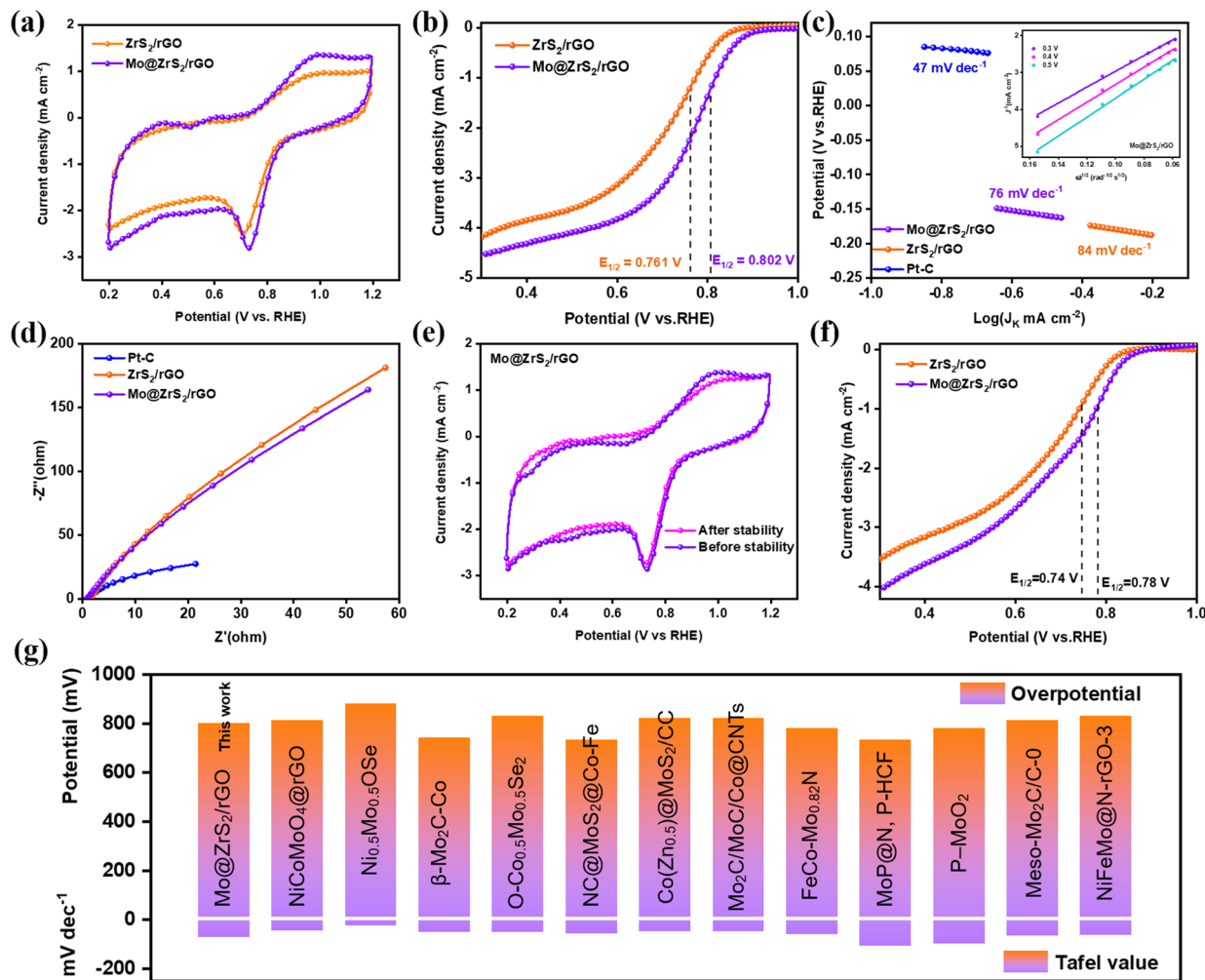


Fig. 4 ORR performance of  $\text{ZrS}_2/\text{rGO}$  and  $\text{Mo@ZrS}_2/\text{rGO}$  electrocatalysts in 0.1 M KOH solution saturated with  $\text{O}_2$ : (a) CV curves, (b) LSV curves, (c) Tafel slopes (inset image; K–L plots of the  $\text{Mo@ZrS}_2/\text{rGO}$  electrocatalyst), and (d) EIS spectra. After the cycling stability test at a speed of 1600 rpm in 0.1 M KOH solution saturated with  $\text{O}_2$ : (e) CV curves and (f) LSV curves. (g) Comparison table for recently reported articles with overpotential and Tafel values.

values (0.94 V and 0.84 V) (see in Fig. 4g and Table S1† for a comparison study). Furthermore, the limiting current ( $J_L$ ) at  $\text{Mo@ZrS}_2/\text{rGO}$  displayed quicker ORR kinetics than Pt–C ( $9.6 \text{ mA cm}^{-2}$ ) and was greater than that at  $\text{ZrS}_2/\text{rGO}$  ( $4.1 \text{ mA cm}^{-2}$ ) and  $\text{Mo@ZrS}_2/\text{rGO}$  ( $4.6 \text{ mA cm}^{-2}$ ).<sup>33</sup> The Tafel slope for a prepared material was then computed, which is crucial for assessing the rate kinetics and figuring out the electrochemical processes of the reaction mechanistic pathway.<sup>46</sup> According to Fig. 4c,  $\text{Mo@ZrS}_2/\text{rGO}$  had a Tafel slope of  $76 \text{ mV dec}^{-1}$ , which was considerably lower than those of  $\text{ZrS}_2/\text{rGO}$  ( $84 \text{ mV dec}^{-1}$ ) and commercial Pt–C ( $47 \text{ mV dec}^{-1}$ ), indicating that reaction rates at  $\text{Mo@ZrS}_2/\text{rGO}$  are faster than those at  $\text{ZrS}_2/\text{rGO}$ .

LSV tests with different rotation speeds and the corresponding computations were carried out to study the mechanism of electron transfer through the ORR (Fig. S4b–d†). The  $\text{Mo@ZrS}_2/\text{rGO}$  modified RDE was subjected to the Koutecky–Levich (K–L) relationship throughout a potential range of

0.3–0.5 V, as shown in the insert image; Fig. 4c, which shows how the current density increased as rotation speed increased. Remarkable linear relationships with almost identical gradients that were equivalent to commercial Pt–C were seen in all of the K–L plots, indicating first-order kinetics behavior for the ORR.<sup>47,48</sup> The K–L equation was used to compute the amount of electrons transferred for the ORR at  $\text{Mo@ZrS}_2/\text{rGO}$ , and the result was 2.12. This indicates that the catalyst has a  $2e^-$  ORR mechanism ( $\text{O}_2 + \text{H}_2\text{O} + 2e^- \rightarrow \text{HO}_2^- + \text{OH}^-$  ( $2e^-$ )).<sup>47</sup> Finally, among the produced catalysts,  $\text{ZrS}_2/\text{rGO}$ ,  $\text{Mo@ZrS}_2/\text{rGO}$ , Pt–C, and electrolytic ions at the interface all showed a comparatively quick energy transfer rate, and  $\text{Mo@ZrS}_2/\text{rGO}$  also showed a low resistance to charge transfer ( $R_{ct}$ ) (Fig. 4d).<sup>9</sup> In addition, the cycling stability of the  $\text{ZrS}_2/\text{rGO}$  and  $\text{Mo@ZrS}_2/\text{rGO}$  was assessed using the CV approach. Fig. 4e and f demonstrates that the current density at  $\text{Mo@ZrS}_2/\text{rGO}$  only decreased by 20 mV of its starting value after 1000 cycles at a scan rate of 500 mV. Fig. S5a–d† show the individual CV and LSV curves of



Pt-C,  $\text{ZrS}_2/\text{rGO}$ , and  $\text{Mo@ZrS}_2/\text{rGO}$  electrocatalysts for assessing before and after cycling stability. Additionally, the  $\text{Mo@ZrS}_2/\text{rGO}$  catalyst's post-morphology was examined, which is depicted in Fig. S7,† for cycling stability following the ORR. This picture demonstrates how the seed-like structure is still intact and how each seed is distributed equally across the rGO nanosheet surface (Fig. S7a–f†). Additionally, the as-produced seed-like structured  $\text{Mo@ZrS}_2/\text{rGO}$  catalysts exhibit stable crystal planes, as shown in the HR-TEM image (Fig. S7g–i†), making them more stable and suitable for future energy storage applications.

### Zn-air battery performance of $\text{ZrS}_2/\text{rGO}$ and $\text{Mo@ZrS}_2/\text{rGO}$ nanocatalysts

Because  $\text{ZrS}_2/\text{rGO}$ ,  $\text{Mo@ZrS}_2/\text{rGO}$ , and Pt-C have excellent ORR characteristics, rechargeable ZABs were constructed by employing them as air electrodes. As seen in Fig. 5a, the  $\text{Mo@ZrS}_2/\text{rGO}$  electrocatalyst is used as the air cathode in a ZAB, where a Zn plate functions as the anode and zinc acetate (0.2 M) is present in the 6 M KOH electrolyte.<sup>1,9</sup> Using the same setup and the commercial Pt-C +  $\text{IrO}_2$  catalyst, comparative testing was also carried out. As seen in Fig. 5b,c, the open-circuit voltage (OCV) of the liquid ZAB was significantly different from that of  $\text{Mo@ZrS}_2/\text{rGO}$  (1.39 V) and marginally lower than that of Pt-C +  $\text{IrO}_2$ , indicating that Mo enhanced the electrocatalytic activity of the seed structure catalyst. Additionally, as illustrated in Fig. 5c, a green light-emitting

device (LED) could be illuminated by joining two liquid ZABs with compared OCV.

The  $\text{Mo@ZrS}_2/\text{rGO}$ -based ZAB demonstrated a higher voltage platform than Pt-C +  $\text{IrO}_2$  when both were exposed to the same current densities. As the current densities increase, the discharge voltage differential becomes increasingly noticeable. Furthermore, the  $\text{Mo@ZrS}_2/\text{rGO}$  battery exhibits a specific capacity and an associated energy density (measured in relation to the mass of Zn consumed) of  $807.9 \text{ mA h g}^{-1}$  (Fig. 5d), which is considerably greater than those of  $\text{ZrS}_2/\text{rGO}$  ( $559 \text{ mA h g}^{-1}$ ) and Pt-C +  $\text{IrO}_2$  ( $762 \text{ mA h g}^{-1}$ ). This means that a variety of electronic gadgets can make use of the created Zn-air batteries. Because  $\text{Mo@ZrS}_2/\text{rGO}$  electrocatalysts exhibit stronger ORR catalytic activity (Table S1†), charging and discharging polarization curves (Fig. S6c and d†) demonstrate a smaller voltage difference in comparison with the  $\text{Mo@ZrS}_2/\text{rGO}$  and Pt-C +  $\text{IrO}_2$  catalyst. The discharge polarization curves and the corresponding power densities of Zn-air batteries are also shown in Fig. 5e and f and S6a and b.† It has been seen that the  $\text{Mo@ZrS}_2/\text{rGO}$  electrocatalyst outperformed the  $\text{ZrS}_2/\text{rGO}$  and comparable Pt-C +  $\text{IrO}_2$  electrodes, with the highest power density of  $128.6 \text{ mW cm}^{-2}$ , compared to  $103.3$  and  $223 \text{ mW cm}^{-2}$ .

Next, one of the most important characteristics of zinc-air batteries is their ability to withstand prolonged charge-discharge cycles, which is essential for assessing the rechargeability of air electrodes.<sup>33,49</sup> Because of the cathodic  $\text{Mo@ZrS}_2/\text{rGO}$  electrocatalyst, the ZAB charge-discharge potential curve exhibits remark-

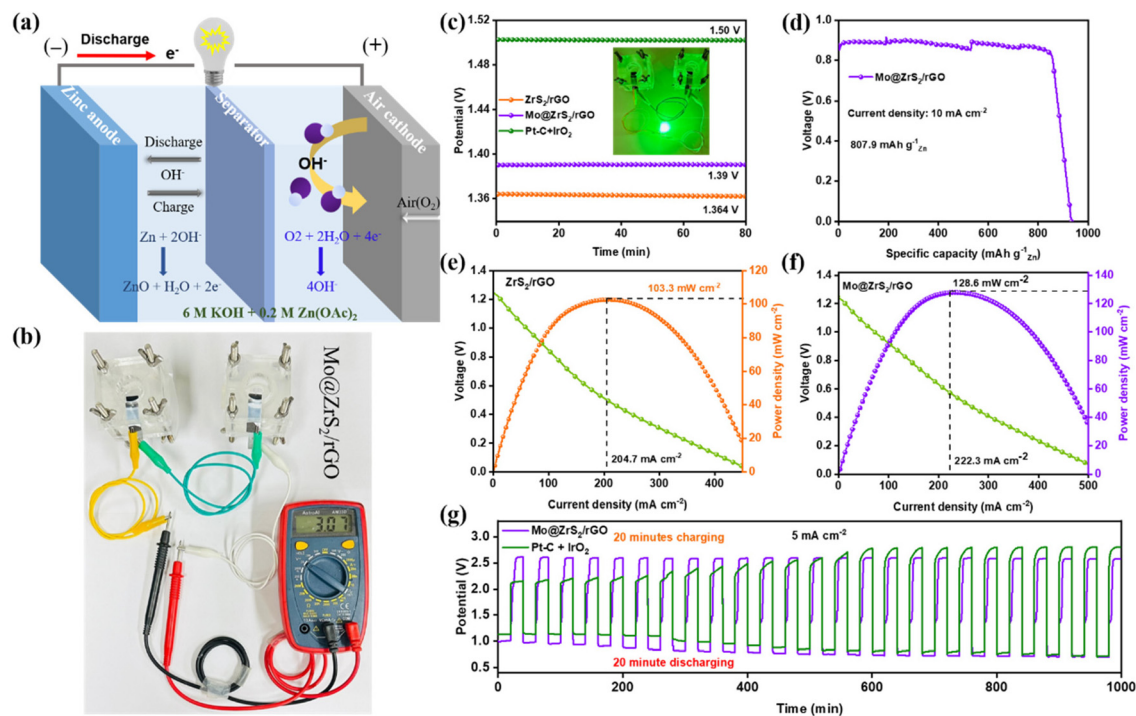
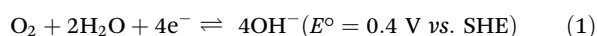


**Fig. 5** (a) Schematic illustration of the ZAB setup, (b) image of the battery with an OCV, (c) OCV curve with an inset image of using LED light in ZABs, (d) specific capacity curve of the  $\text{Mo@ZrS}_2/\text{rGO}$  air cathode electrode, (e and f) power density curves of  $\text{ZrS}_2/\text{rGO}$  and  $\text{Mo@ZrS}_2/\text{rGO}$  air cathode electrodes, (g) galvanostatic charge-discharge curve at a current density of  $5 \text{ mA cm}^{-2}$  of commercial Pt-C +  $\text{IrO}_2$  and  $\text{Mo@ZrS}_2/\text{rGO}$  air cathode electrodes, respectively.

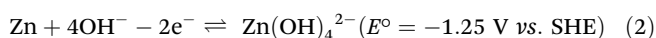
able stability for 25 cycles up to 16 h. As illustrated in Fig. 5g, the charge–discharge cycling experiments were conducted at a steady current density of  $5 \text{ mA cm}^{-2}$ , with the discharge lasting 20 minutes and the charge lasting an extra 20 minutes. The Pt–C + IrO<sub>2</sub> cathode, on the other hand, has a stability period of over 16 hours. Furthermore, the Mo@ZrS<sub>2</sub>/rGO electrocatalyst performed better than the Pt–C + IrO<sub>2</sub> electrocatalyst at an average current density of  $5 \text{ mA cm}^{-2}$ , with an electrode voltage gap between charge and discharge cycles of 1.6 V compared to 1.01 V for the Pt–C + IrO<sub>2</sub> cathode (Fig. S6c and d†). This further implies that Mo@ZrS<sub>2</sub>/rGO is a bifunctional catalyst for cyclability and ORR activities that is highly effective. It is noteworthy that in the presence of Mo, ZrS<sub>2</sub>/rGO exhibits a constant charge voltage.

Lastly, the redox reactions that take place in alkaline solutions across the cathode and anode can be used to characterize the complete electrochemical system (eqn (1)–(3)).

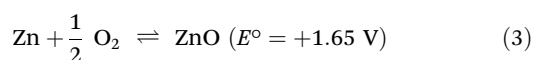
Cathodic reaction:



Anodic reaction:



Overall reaction:



## 4. Conclusion

A unique seed-like structure of ZrS<sub>2</sub> on rGO was generated and structural deformation was restricted by the doped Mo atom on the ZrS<sub>2</sub> surface. This was achieved by a simple hydrothermal-based annealing process. XRD, XPS, and TEM characterization methods were used to examine the produced catalysts. The resulting seed-like structure was used in ZABs and showed remarkable catalytic capabilities for ORRs. Mo@ZrS<sub>2</sub>/rGO has the longest cycling stability (at a scan rate of 500 mV) and the lowest half-wave potential (0.80 V) for the ORR in a 0.1 M KOH solution. In addition, Mo@ZrS<sub>2</sub>/rGO showed remarkable performance as an air cathode in zinc–air batteries due to its longer cycling stability, higher specific capacity ( $807.9 \text{ mA h g}^{-1}_{\text{Zn}}$ ), higher power density ( $128.6 \text{ mW cm}^{-2}$ ), and higher OCV (1.39 V). Lastly, this is the first time that Mo-doped zirconium sulfide catalyst has been developed with a seed-like structure, and the findings offer a variety of prospects for further research and development to increase catalytic activity and incorporate novel features for energy storage and conversion applications.

## Author contributions

Ramasamy Santhosh Kumar: conceptualization, experimental, investigation, formal analysis, and writing – review of the original draft. Dilmurod Sayfiddinov and S. Tamilarasi: character-

ization and data visualization. Dong Jin Yoo: data visualization, review of the original draft, funding acquisition, and research supervision of the work.

## Data availability

The data supporting the findings of this study are available within the article and its ESI.† Source data are provided in this paper.

Request can be made to the corresponding author for accessing the data.

## Conflicts of interest

The authors declare no competing interests.

## Acknowledgements

This research was supported by the “Regional Innovation Strategy (RIS)” through the National Research Foundation of Korea (NRF) funded by the Ministry of Education (MOE) (2024RIS-008). This research was supported by “Regional Integrated Hydrogen Industry Human Resource Development (jeonbuk National University) Program” grant funded by the Ministry of Trade, Industry and Energy (H2 Korea).

## References

- 1 J. Balamurugan, P. M. Austeria, J. B. Kim, E.-S. Jeong, H.-H. Huang, D. H. Kim, N. Koratkar and S. O. Kim, Electrocatalysts for Zinc–Air Batteries Featuring Single Molybdenum Atoms in a Nitrogen-Doped Carbon Framework, *Adv. Mater.*, 2023, **35**, 2302625.
- 2 J. Zhang, Z. Zhao, Z. Xia and L. Dai, A metal-free bifunctional electrocatalyst for oxygen reduction and oxygen evolution reactions, *Nat. Nanotechnol.*, 2015, **10**, 444–452.
- 3 Z. P. Cano, D. Banham, S. Ye, A. Hintennach, J. Lu, M. Fowler and Z. Chen, Batteries and fuel cells for emerging electric vehicle markets, *Nat. Energy*, 2018, **3**, 279–289.
- 4 H. Zhang, G. Meng, Q. Liu, Y. Luo, M. Niederberger, L. Feng, J. Luo and X. Liu, Metal Phosphorous Chalcogenide: A Promising Material for Advanced Energy Storage Systems, *Small*, 2023, **19**, 2303165.
- 5 W. Sun, F. Wang, B. Zhang, M. Zhang, V. Küpers, X. Ji, C. Theile, P. Bieker, K. Xu, C. Wang and M. Winter, A rechargeable zinc-air battery based on zinc peroxide chemistry, *Science*, 2021, **371**, 46–51.
- 6 Y. Ma, S. Tang, H. Wang, Y. Liang, D. Zhang, X. Xu, Q. Wang and W. Li, Bimetallic ZIFs-derived electrospun carbon nanofiber membrane as bifunctional oxygen electrocatalyst for rechargeable zinc-air battery, *J. Energy Chem.*, 2023, **83**, 138–149.



- 7 M. Luo and M. T. M. Koper, A kinetic descriptor for the electrolyte effect on the oxygen reduction kinetics on Pt (111), *Nat. Catal.*, 2022, **5**, 615–623.
- 8 A. Grimaud, A. Demortière, M. Saubanère, W. Dachraoui, M. Duchamp, M.-L. Doublet and J.-M. Tarascon, Erratum: Activation of surface oxygen sites on an iridium-based model catalyst for the oxygen evolution reaction, *Nat. Energy*, 2017, **2**, 17002.
- 9 R. S. Kumar, P. Mannu, S. Prabhakaran, T. T. T. Nga, Y. Kim, D. H. Kim, J.-L. Chen, C.-L. Dong and D. J. Yoo, Trimetallic Oxide Electrocatalyst for Enhanced Redox Activity in Zinc–Air Batteries Evaluated by In Situ Analysis, *Adv. Sci.*, 2023, **10**, 2303525.
- 10 F. Zhang, Y. Zhu, Y. Zhong, J. Zou, Y. Chen, L. Zu, Z. Wang, J. J. Hinsch, Y. Wang, L. Zhang, Z. Shao and H. Wang, Tuning the charge distribution and crystal field of iron single atoms via iron oxide integration for enhanced oxygen reduction reaction in zinc-air batteries, *J. Energy Chem.*, 2023, **85**, 154–163.
- 11 J. Ban, H. Xu, G. Cao, Y. Fan, W. K. Pang, G. Shao and J. Hu, Synergistic Effects of Phase Transition and Electron-Spin Regulation on the Electrocatalysis Performance of Ternary Nitride, *Adv. Funct. Mater.*, 2023, **33**, 2300623.
- 12 S. Yi, R. Xin, X. Li, Y. Sun, M. Yang, B. Liu, H. Chen, H. Li and Y. Liu, “*Setaria viridis*”-like cobalt complex derived Co/N-doped carbon nanotubes as efficient ORR/OER electrocatalysts for long-life rechargeable Zn–air batteries, *Nanoscale*, 2023, **15**, 16612–16618.
- 13 A. Singh, R. Sharma and A. Halder, Flexible solid-state Zn–air battery based on polymer-oxygen-functionalized g-C<sub>3</sub>N<sub>4</sub> composite membrane, *Nanoscale*, 2024, **16**, 4157–4169.
- 14 Y.-P. Deng, Y. Jiang, R. Liang, S.-J. Zhang, D. Luo, Y. Hu, X. Wang, J.-T. Li, A. Yu and Z. Chen, Dynamic electrocatalyst with current-driven oxyhydroxide shell for rechargeable zinc-air battery, *Nat. Commun.*, 2020, **11**, 1952.
- 15 L. Liu, X. Zhang, F. Yan, B. Geng, C. Zhu and Y. Chen, Self-supported N-doped CNT arrays for flexible Zn–air batteries, *J. Mater. Chem. A*, 2020, **8**, 18162–18172.
- 16 R. J. Toh, A. Y. S. Eng, Z. Sofer, D. Sedmidubsky and M. Pumera, Ternary Transition Metal Oxide Nanoparticles with Spinel Structure for the Oxygen Reduction Reaction, *ChemElectroChem*, 2015, **2**, 982–987.
- 17 R. Santhosh Kumar, P. Muthu Austeria, C. Sagaya Selvam Neethinathan, S. Ramakrishnan, K. Sekar, A. R. Kim, D. H. Kim, P. J. Yoo and D. J. Yoo, Highly mixed high-energy d-orbital states enhance oxygen evolution reactions in spinel catalysts, *Appl. Surf. Sci.*, 2023, **641**, 158469.
- 18 M. Chisaka, A. Ishihara, K.-I. Ota and H. Muramoto, Synthesis of carbon-supported titanium oxynitride nanoparticles as cathode catalyst for polymer electrolyte fuel cells, *Electrochim. Acta*, 2013, **113**, 735–740.
- 19 V. Kashyap and S. Kurungot, Zirconium-Substituted Cobalt Ferrite Nanoparticle Supported N-doped Reduced Graphene Oxide as an Efficient Bifunctional Electrocatalyst for Rechargeable Zn–Air Battery, *ACS Catal.*, 2018, **8**, 3715–3726.
- 20 N. Logeshwaran, I. R. Panneerselvam, S. Ramakrishnan, R. S. Kumar, A. R. Kim, Y. Wang and D. J. Yoo, Quasi-hexagonal Platinum Nanodendrites Decorated over CoS<sub>2</sub>-N-Doped Reduced Graphene Oxide for Electro-Oxidation of C1-, C2-, and C3-Type Alcohols, *Adv. Sci.*, 2022, **9**, 2105344.
- 21 H. Yang, B. Wang, H. Li, B. Ni, K. Wang, Q. Zhang and X. Wang, Trimetallic Sulfide Mesoporous Nanospheres as Superior Electrocatalysts for Rechargeable Zn–Air Batteries, *Adv. Energy Mater.*, 2018, **8**, 1801839.
- 22 J. Zhang, X. Bai, T. Wang, W. Xiao, P. Xi, J. Wang, D. Gao and J. Wang, Bimetallic Nickel Cobalt Sulfide as Efficient Electrocatalyst for Zn–Air Battery and Water Splitting, *Nano-Micro Lett.*, 2019, **11**, 2.
- 23 Z. Wang, C. Li, Y. Liu, Y. Wu, S. Zhang and C. Deng, Atomically dispersed Fe–Ni dual sites in heteroatom doped carbon tyres for efficient oxygen electrocatalysis in rechargeable Zn–Air battery, *J. Energy Chem.*, 2023, **83**, 264–274.
- 24 M. Kumar and T. C. Nagaiah, A multifunctional cobalt iron sulfide electrocatalyst for high performance Zn–air batteries and overall water splitting, *J. Mater. Chem. A*, 2022, **10**, 4720–4730.
- 25 M. Wang, L. Zhang, Y. He and H. Zhu, Recent advances in transition-metal-sulfide-based bifunctional electrocatalysts for overall water splitting, *J. Mater. Chem. A*, 2021, **9**, 5320–5363.
- 26 H. Chen, Z. Yu, Y. Hou, R. Jiang, J. Huang, W. Tang, Z. Cao, B. Yang, C. Liu and H. Song, Double MOF gradually activated S bond induced S defect rich MILN-based Co(z)-NiMoS for efficient electrocatalytic overall water splitting, *Nanoscale*, 2021, **13**, 20670–20682.
- 27 X. Cao, S. Zheng, T. Wang, F. Lin, J. Li and L. Jiao, N-doped ZrO<sub>2</sub> nanoparticles embedded in a N-doped carbon matrix as a highly active and durable electrocatalyst for oxygen reduction, *Fundam. Res.*, 2022, **2**, 604–610.
- 28 X. Zhao, J. Wang, J. Wang, M. Yang, C. Yan, G. Zou, J. S. Tse, C. Fernandez and Q. Peng, Atomically dispersed quintuple nitrogen and oxygen co-coordinated zirconium on graphene-type substrate for highly efficient oxygen reduction reaction, *Cell Rep. Phys. Sci.*, 2022, **3**, 100773.
- 29 H. Sudrajat and S. Babel, Comparison and mechanism of photocatalytic activities of N–ZnO and N–ZrO<sub>2</sub> for the degradation of rhodamine 6G, *Environ. Sci. Pollut. Res.*, 2016, **23**, 10177–10188.
- 30 S. Tamilarasi, R. S. Kumar, K.-B. Cho, C.-J. Kim and D. J. Yoo, High-performance electrochemical detection of glucose in human blood serum using a hierarchical NiO<sub>2</sub> nanostructure supported on phosphorus doped graphene, *Mater. Today Chem.*, 2023, **34**, 101765.
- 31 R. Santhosh Kumar, K. Govindan, S. Ramakrishnan, A. R. Kim, J.-S. Kim and D. J. Yoo, Fe<sub>3</sub>O<sub>4</sub> nanorods decorated on polypyrrole/reduced graphene oxide for electrochemical detection of dopamine and photocatalytic degradation of acetaminophen, *Appl. Surf. Sci.*, 2021, **556**, 149765.

- 32 Y. Liang, Y. Li, H. Wang, J. Zhou, J. Wang, T. Regier and H. Dai,  $\text{Co}_3\text{O}_4$  nanocrystals on graphene as a synergistic catalyst for oxygen reduction reaction, *Nat. Mater.*, 2011, **10**, 780–786.
- 33 R. S. Kumar, S. Prabhakaran, S. Ramakrishnan, S. C. Karthikeyan, A. R. Kim, D. H. Kim and D. J. Yoo, Developing Outstanding Bifunctional Electrocatalysts for Rechargeable Zn-Air Batteries Using High-Purity Spinel-Type  $\text{ZnCo}_2\text{Se}_4$  Nanoparticles, *Small*, 2023, **19**, 2207096.
- 34 R. Santhosh Kumar, S. Ramakrishnan, S. Prabhakaran, A. R. Kim, D. R. Kumar, D. H. Kim and D. J. Yoo, Structural, electronic, and electrocatalytic evaluation of spinel transition metal sulfide supported reduced graphene oxide, *J. Mater. Chem. A*, 2022, **10**, 1999–2011.
- 35 R. Santhosh Kumar, S. C. Karthikeyan, S. Ramakrishnan, S. Vijayapradeep, A. R. Kim, J.-S. Kim and D. J. Yoo, Anion dependency of spinel type cobalt catalysts for efficient overall water splitting in an acid medium, *Chem. Eng. J.*, 2023, **451**, 138471.
- 36 S. B. Patil, M. S. Raghu, B. Kishore and G. Nagaraju, Enhanced electrochemical performance of few-layered  $\text{MoS}_2$ -rGO nanocomposite for lithium storage application, *J. Mater. Sci.: Mater. Electron.*, 2019, **30**, 316–322.
- 37 A. Smirnov, N. W. Solís Pinargote, N. Peretyagin, Y. Pristinskiy, P. Peretyagin and J. F. Bartolomé, Zirconia Reduced Graphene Oxide Nano-Hybrid Structure Fabricated by the Hydrothermal Reaction Method, *Materials*, 2020, **13**, 687.
- 38 P. Fadojutimi, C. Masemola, M. Maubane-Nkadimeng, E. Linganis, Z. Tetana, J. Moma, N. Moloto and S. Gqoba, Room temperature sensing of primary alcohols via polyaniline/zirconium disulphide, *Heliyon*, 2023, **9**, e16216.
- 39 J. Chen, Y. Xia, J. Yang and B. Chen, Fabrication of monolayer  $\text{MoS}_2$ /rGO hybrids with excellent tribological performances through a surfactant-assisted hydrothermal route, *Appl. Phys. A*, 2018, **124**, 430.
- 40 G. Tai, T. Zeng, J. Yu, J. Zhou, Y. You, X. Wang, H. Wu, X. Sun, T. Hu and W. Guo, Fast and large-area growth of uniform  $\text{MoS}_2$  monolayers on molybdenum foils, *Nanoscale*, 2016, **8**, 2234–2241.
- 41 H. Yu, C. Ma, B. Ge, Y. Chen, Z. Xu, C. Zhu, C. Li, Q. Ouyang, P. Gao, J. Li, C. Sun, L. Qi, Y. Wang and F. Li, Three-Dimensional Hierarchical Architectures Constructed by Graphene/ $\text{MoS}_2$  Nanoflake Arrays and Their Rapid Charging/Discharging Properties as Lithium-Ion Battery Anodes, *Chem. – Eur. J.*, 2013, **19**, 5818–5823.
- 42 A. Wang, S. Gao, J. Yan, C. Zhao, M. Yu and W. Wang, Vacancy-modified bimetallic  $\text{FeMoSx/CoNiPx}$  heterostructure array for efficient seawater splitting and Zn-air battery, *J. Energy Chem.*, 2023, **81**, 533–542.
- 43 J. Zhou, X. Zha, F. Y. Chen, Q. Ye, P. Eklund, S. Du and Q. Huang, A Two-Dimensional Zirconium Carbide by Selective Etching of  $\text{Al}_3\text{C}_3$  from Nanolaminated  $\text{Zr}_3\text{Al}_3\text{C}_5$ , *Angew. Chem., Int. Ed.*, 2016, **55**, 5008–5013.
- 44 A. P. Rizzato, C. V. Santilli, S. H. Pulcinelli, Y. Messaddeq and P. Hammer, XPS Study of the Corrosion Protection of Fluorozirconate Glasses Dip-Coated with  $\text{SnO}_2$  Transparent Thin Films, *J. Sol-Gel Sci. Technol.*, 2004, **32**, 155–160.
- 45 M. Otomo, M. Hamada, R. Ono, I. Muneta, K. Kakushima, K. Tsutsui and H. Wakabayashi, Chemical states of PVD-ZrS<sub>2</sub> film underneath scaled high-k film with self-oxidized  $\text{ZrO}_2$  film as interfacial layer, *Jpn. J. Appl. Phys.*, 2023, **62**, SC1015.
- 46 T. Shinagawa, A. T. Garcia-Esparza and K. Takanabe, Insight on Tafel slopes from a microkinetic analysis of aqueous electrocatalysis for energy conversion, *Sci. Rep.*, 2015, **5**, 13801.
- 47 R. Zhou, Y. Zheng, M. Jaroniec and S.-Z. Qiao, Determination of the Electron Transfer Number for the Oxygen Reduction Reaction: From Theory to Experiment, *ACS Catal.*, 2016, **6**, 4720–4728.
- 48 T. Wang, Q. Zhang, K. Lian, G. Qi, Q. Liu, L. Feng, G. Hu, J. Luo and X. Liu, Fe nanoparticles confined by multiple-heteroatom-doped carbon frameworks for aqueous Zn-air battery driving  $\text{CO}_2$  electrolysis, *J. Colloid Interface Sci.*, 2024, **655**, 176–186.
- 49 S. Gao, X. Wang, X. Liu, C. Guo, Q. Liu and G. Hu, Recent progress in iron-series-element-based electrocatalysts for Zn-air batteries, *Mater. Chem. Front.*, 2024, **8**, 485–506.